Development and Preliminary Analysis of a MATLAB/Simulink-Based System-Scale Model of a Coupled High-Temperature Gas-Cooled Reactor–Solid Oxide Electrolysis Cell System

Jiwon Ahn and Hyoung Kyu Cho*
Department of Nuclear Eng., Seoul National Univ., 1 Gwanak-ro, Gwanak-gu, Seoul 08826
**Corresponding author: chohk@snu.ac.kr*

***Keywords : HTGR; SOEC; Dynamic modeling; Nuclear hydrogen production.**

1. Introduction

Hydrogen production using low-carbon energy sources has received increasing attention for decarbonizing energy-intensive industries. Among available technologies, solid oxide electrolysis cells (SOECs) operate at elevated temperatures and can use externally supplied heat to reduce the electrical energy required for steam electrolysis [1]. This makes coupling with high-temperature heat sources attractive, and high-temperature gas-cooled reactors (HTGRs) are well suited for this purpose because of their high coolant outlet temperature and capability for supplying process heat [1,2].

Previous studies have examined nuclear-assisted hydrogen production and HTGR–SOEC thermodynamic performance, whereas comparatively fewer studies have addressed the transient behavior of coupled steam-supply systems [3,4]. Because steam delivery depends on the coupled thermal and hydraulic responses of heat exchangers, the steam generator, and feedwater system, these components were modeled dynamically. Fig. 1 shows the conceptual HTGR–SOEC configuration and its principal heat-transfer, process-gas, and recycle paths. Reactor heat is transferred through the intermediate heat exchanger (IHX) to the intermediate helium loop, which supplies heat to the multi-stream heat exchanger (MHX) and once-through steam generator (OTSG). The water pump supplies feedwater, while the SOEC represents electrochemical hydrogen production. Heat recovery from the SOEC exhaust streams is integrated with feedwater and inlet-stream preheating, while recovered liquid water and a controlled fraction of the H_2-rich gas are recycled to the feedwater train and SOEC cathode inlet, respectively.

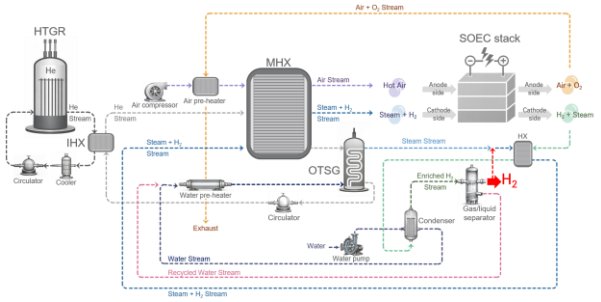


Fig. 1. Conceptual configuration of the HTGR–SOEC hydrogen production system.

2. Model description

2.1. System model

Fig. 2 shows the configuration represented in the present model. Reactor heat is transferred through the IHX to the intermediate helium loop, which successively supplies heat to the MHX and OTSG. On the water/steam side, feedwater is pressurized by the water pump and preheated in the condenser and second preheating heat exchanger (PHX2) before entering the OTSG. The generated steam is further heated through the recuperative heat exchanger (RHX) and MHX, followed by pressure reduction through a fixed nozzle before SOEC entry. On the air side, compressed air is preheated in the first preheating heat exchanger (PHX1) and subsequently heated in the MHX. At the SOEC outlet, the cathode H_2/H_2O stream passes through the RHX, condenser, and gas/liquid separator, whereas the Air–O_2 exhaust supplies heat to PHX2. A fraction of the recovered liquid water is returned to the water pump inlet. Part of the H_2-rich separator gas is also recirculated, with the recycle flow adjusted to achieve the prescribed H_2-to-steam molar ratio at the SOEC inlet.

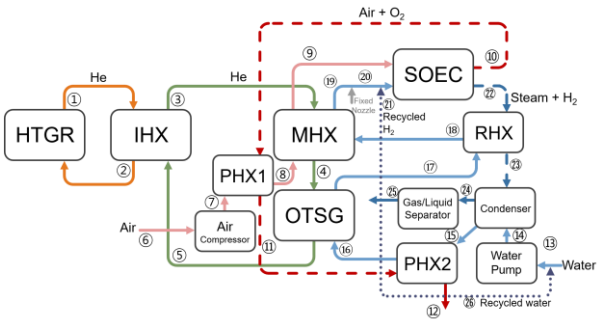


Fig. 2. HTGR–SOEC system schematic.

To assess the thermodynamic performance of the integrated configuration, system-level energy and exergy analyses were performed using the stream conditions and power requirements obtained from the component models. The overall energy efficiency was evaluated on an H_2 lower-heating-value (LHV) basis, accounting for the reactor thermal input and the externally supplied SOEC and auxiliary power. Stream exergy was evaluated from physical and, where applicable, chemical contributions relative to an environmental reference state, while electrical work was treated as exergy. The overall

exergy efficiency was defined as the H_2-product exergy relative to the total exergy supplied to the system.

2.2. Component models

Each component was modeled in MATLAB/Simulink using lumped-parameter formulations based on mass and energy conservation to enable system-level dynamic simulation.

$$\frac{dm}{dt} = \sum \dot{m}_{in} - \sum \dot{m}_{out} + \dot{m}_{src} \quad (1)$$

where m is the mass within the control volume, and $\dot{m}_{src}$ represents a source or sink term when applicable.

$$\frac{dU}{dt} = \sum \dot{m}_{i,in} h_{i,in} - \sum \dot{m}_{i,out} h_{i,out} + \dot{Q} - \dot{W} \quad (2)$$

where U is the internal energy, h is the specific enthalpy, and $\dot{Q}$ and $\dot{W}$ denote the heat-transfer and work rates, respectively. These conservation equations form the common basis of the component models, with additional relations introduced according to the dominant physics of each component. Within this framework, the HTGR couples reactor neutronics and reactivity feedback with the thermal-hydraulic balances in a unified dynamic model [5]. Reactor power is calculated using the point-kinetics equations with delayed neutrons, accounting for time-dependent neutron population and core thermal feedback:

$$\frac{dn(t)}{dt} = \frac{\rho-\beta}{\Lambda} n + \sum_{i=1}^{6} \lambda_i C_i(t) \quad (3)$$

where n is the normalized neutron population, ρ is the reactivity, β is the total delayed-neutron fraction, Λ is the prompt neutron generation time, and C_i and λ_i are the concentration and decay constant of the i-th delayed-neutron precursor group, respectively. The precursor concentrations evolve according to

$$\frac{dC_i(t)}{dt} = \frac{\beta_i}{\Lambda} n(t) - \lambda_i C_i(t), \quad i = 1, \dots, 6 \quad (4)$$

where β_i is the delayed-neutron fraction of the i-th group. The resulting neutron population determines the reactor thermal power, which is supplied to the thermal-hydraulic model as the core heat source. The corresponding thermal response is then fed back to the kinetics model through the fuel- and moderator-temperature reactivity coefficients:

$$\rho(t) = \alpha_D \Delta T_f + \alpha_m \Delta T_m + \alpha_P \Delta P + \alpha_H \Delta H_{cr} \quad (5)$$

where ΔT_f, ΔT_m, ΔP, and ΔH_{cr} are deviations in fuel temperature, moderator temperature, pressure, and control-rod height from their reference values, respectively. Here, α_D is the fuel-temperature Doppler reactivity coefficient, while α_m, α_P, and α_H are the moderator-temperature, pressure, and control-rod reactivity coefficients, respectively. The thermal-hydraulic states provide the temperature and pressure feedback, while the control-rod position supplies the externally actuated contribution, thereby coupling the neutronic, thermal-hydraulic, and control responses.

The heat-exchanger models combine the common mass and energy balances with heat-transfer relations based on the effectiveness–NTU method. In the present system, the IHX, MHX, RHX, and PHX1 are represented using PCHE-based formulations. Printed circuit heat exchangers (PCHEs) are adopted because their compact diffusion-bonded structure provides a high heat-transfer area density and is suitable for high-temperature, high-pressure service [6]. Their alternating channels separate the fluid streams through thin metallic walls. A reduced-order counter-current configuration is used to represent this structure, maintaining a favorable thermal driving force along the flow direction and effective use of the available heat-transfer area. Detailed channel-scale fields are not resolved; instead, the dominant thermal-hydraulic behavior is represented through the stream heat-capacity rates, overall conductance, and pressure-drop relations. Based on this reduced-order representation, the heat-transfer rate is calculated as

$$\dot{Q} = \varepsilon C_{min} \left(T_{h,in} - T_{c,in} \right) \quad (6)$$

where $C = \dot{m} C_p$, C_{min} is the smaller heat-capacity rate, and ε is evaluated from the conventional counter-current effectiveness–NTU relation. The number of transfer units is defined as

$$NTU = \frac{UA}{C_{min}} \quad (7)$$

where UA represents the overall thermal conductance and is determined from the convective heat transfer on both fluid sides and conduction through the separating wall. For the PCHE geometry, the heat-transfer coefficients and pressure losses are evaluated using the local fluid properties, Reynolds number, and geometric parameters including the hydraulic diameter, pitch, and channel angle [6]. Using this reduced-order representation, the IHX, RHX, and PHX1 are modeled as two-stream PCHEs, with the fluid pairs assigned according to their respective system functions. The IHX transfers heat between the primary and intermediate helium loops, whereas the RHX and PHX1 recover process heat for steam heating and inlet-stream preheating, respectively. The MHX extends this approach to a three-stream configuration, in which hot helium transfers heat separately to the steam and air streams [7]. Its heat duties are coupled through an overall energy balance so that the heat removed from helium is consistent with the combined heat gained by the two cold streams.

The OTSG converts preheated feedwater into moderately superheated steam using heat supplied by the intermediate helium loop. As shown in Fig. 3 (a), high-pressure helium flows downward through the helical tubes, while water and steam flow upward on the shell

side in a counter-current arrangement. The tube side accommodates the high-pressure helium, whereas the larger shell-side flow area accommodates the volumetric expansion associated with boiling. The upward secondary flow is also aligned with the buoyancy direction during vapor generation. For the dynamic formulation, the helium and tube wall are discretized into nine fixed axial control volumes, while the secondary side is represented by moving thermodynamic regions, as illustrated in Fig. 3 (b).

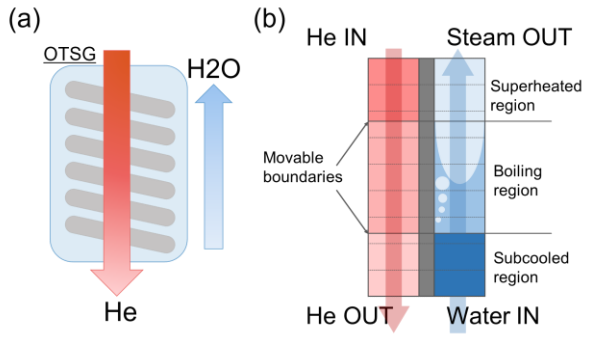


Fig. 3. (a) Schematic of the OTSG configuration and (b) moving thermodynamic regions.

The secondary side is represented by subcooled, two-phase, and superheated regions whose lengths vary with the thermal-hydraulic state [8,9]. The boundaries between these regions are determined from the local saturation conditions:

$$(8) \quad h(z_{\mathrm{boil}}) = h_f(P_{sec}), \qquad h(z_{\mathrm{dry}}) = h_g(P_{sec})$$

where z_{boil} and z_{dry} denote the onset of boiling and the boundary to the superheated region, respectively. Conservation over each time-varying region is formulated using the Leibniz integral rule:

$$(9) \quad \frac{d}{dt}\int_{z_1}^{z_2} \phi \, dz = \int_{z_1(t)}^{z_2(t)} \frac{\partial \phi}{\partial t} \, dz + \phi_2 \dot{z}_2 - \phi_1 \dot{z}_1$$

where ϕ denotes a conserved quantity per unit length. The boundary-motion terms account for changes in the region length as z_1 and z_2 move. The resulting conservation equations are solved with the saturation constraints in Eq. (8), allowing the phase boundaries to evolve with the transient state rather than being prescribed independently. The moving secondary-side regions are thermally coupled to the fixed helium and tube-wall control volumes to evaluate the local thermal response and interfacial heat transfer. Heat transfer on the helium side is evaluated using the Mori–Nakayama correlation [10] for flow in helical tubes, while the secondary-side treatment depends on the local phase and boiling regime, as summarized in Table 1. For the secondary side, the Rohsenow correlation is used for nucleate boiling and the Zuber correlation for critical heat flux (CHF). Post-CHF heat transfer is approximated by interpolation toward the minimum film-boiling (MFB) condition estimated using the Berenson correlation, followed by the Bromley correlation for stable film boiling. These correlations provide a reduced-order representation of the principal boiling regimes rather than a detailed prediction of local two-phase phenomena.

Table 1. OTSG secondary-side correlations.

Secondary-side condition	Correlation / treatment
Subcooled water	Dittus–Boelter
Nucleate boiling	Rohsenow [11]
Critical heat flux (CHF)	Zuber [12]
Transition boiling	CHF–MFB interpolation
MFB condition	Berenson [13]
Stable film boiling	Bromley [14]
Superheated steam	Dittus–Boelter

A hydraulic relation is also required to close the pressure–flow response of the model. For a flow path with variable effective length, the momentum balance can be written in compact form as

$$(10) \quad \frac{dW}{dt} = \frac{A}{L}(\Delta P - \sum \Delta P_{loss}) - \frac{W}{L}\frac{dL}{dt}$$

where $\sum \Delta P_{loss}$ includes frictional, gravitational, acceleration, and local-loss contributions. The final term accounts for changes in the effective flow-path length associated with boundary motion.

A centrifugal-pump model is used to supply feedwater to the OTSG. In the reduced-order formulation, the actual flow rate is determined from the momentum balance of the pump and equivalent discharge line rather than being imposed directly:

$$(11) \quad \frac{L}{A}\frac{dW}{dt} = \Delta P_{\mathrm{net}} - \Delta P_{loss}$$

where $\Delta P_{\mathrm{net}} = \Delta P_{pump} + P_{source} - P_{down} - \rho g \Delta z$ and ΔP_{loss} represents the hydraulic resistance of the flow path. To account for the transient response of the pump, the pump pressure rise is obtained from a centrifugal-pump Q-H characteristic. The shaft dynamics are represented by

$$(12) \quad J_{eq}\frac{d\omega}{dt} = \tau_{motor} - \tau_{pump} - \tau_{fric}$$

Here, J_{eq} and ω are the equivalent rotational inertia and shaft speed, while the three torque terms represent the motor input, hydraulic load, and mechanical friction, respectively. Thus, both flow and shaft speed evolve dynamically from the corresponding momentum balances.

PHX2 is introduced to recover sensible heat from the Air–O_2 exhaust before it is rejected, thereby preheating feedwater upstream of the OTSG. It is modeled as a four-control-volume counter-current shell-and-tube heat exchanger, with liquid water on the tube side and the

Air–O_2 stream on the shell side. The water remains subcooled throughout PHX2, leaving evaporation and subsequent superheating to the downstream OTSG. Since the mass and energy balances are common to the component models, the assumption of the model PHX2-specific closure is given by the single-phase convective heat-transfer relation. For the tube-side water, the heat-transfer coefficient is evaluated using the Gnielinski correlation [15],

$$Nu_w = \frac{(f_w/8)(Re_w - 1000)Pr_w}{1+12.7(f_w/8)^{1/2}\left(Pr_w^{2/3}-1\right)} \quad (13)$$

where Nu_w, Re_w, and Pr_w are the Nusselt, Reynolds, and Prandtl numbers of the water, respectively, and f_w is the Darcy friction factor.

The condenser is modeled separately to remove water from the H_2/H_2O cathode exhaust before downstream gas/liquid separation. In contrast to PHX2, which transfers sensible heat between single-phase streams, the condenser couples heat removal with H_2O condensation in the presence of hydrogen. It also differs from the OTSG, where heat addition drives feedwater through evaporation and superheating. In the condenser, the H_2O phase state is evaluated from saturated-liquid and saturated-vapor properties, with the process- and coolant-side enthalpies treated as dynamic states. The local H_2O quality is determined from pressure–enthalpy property data. To account for the presence of non-condensable H_2, condensation is not determined from the heat duty alone. Instead, the model includes gas-side H_2O mass transfer together with the local saturation condition at the cooled interface. The corresponding mass-transfer coefficient is evaluated using the Chilton–Colburn analogy [16]:

$$k_m = \frac{j_D Re_g Sc^{1/3} D_{AB}}{D_h} \quad (14)$$

where k_m is the H_2O vapor mass-transfer coefficient, j_D is the Chilton–Colburn mass-transfer factor, Re_g is the gas-side Reynolds number, and Sc is the Schmidt number. D_{AB} denotes the binary diffusivity of the H_2–H_2O mixture, and D_h is the hydraulic diameter. The resulting mass transfer governs the transport of H_2O vapor toward the condensing interface, thereby coupling species removal with the condenser thermal response.

The gas/liquid separator is placed downstream of the condenser to recover condensed water from the enriched H_2 stream. It is represented as a zero-dimensional bank of vertical separator modules with a downstream wire-mesh demister, retaining gravity-assisted disengagement while accounting for residual fine-droplet capture. The entrained liquid is represented by three computational droplet classes with diameters of 5, 50, and 300 μm, which are treated as representative model classes rather than a measured droplet-size distribution. The droplet velocity is obtained from a reduced-order momentum balance using the Schiller–Naumann drag relation [17], and the gravity-separation rate is evaluated as

$$\dot{m}_{grav,i} = \frac{\max(v_{d,i} - U_{g,})}{H_{sep}} \dot{m}_{d,i} \quad (15)$$

where $\dot{m}_{d,i}$ is the liquid inventory of droplet class i, $v_{d,i}$ is the modeled downward droplet velocity, U_g is the upward superficial gas velocity, and H_{sep} is the separator height. Coalescence is represented as conservative transfer between droplet classes, while the downstream demister model estimates the captured and penetrated fractions of the residual mist. This reduced-order treatment is intended to represent liquid recovery and carryover at the system level rather than detailed separator-scale two-phase hydrodynamics.

The SOEC model developed in our previous study [18] is adopted with minor modifications for the present system integration. Since its detailed formulation and assessment have been reported previously, only the features relevant to the present analysis are summarized. A single cell is discretized into 5×5 nodes to represent spatial variations in temperature, gas composition, and current density. All nodes share a common cell voltage, while the local current density is determined from the local thermodynamic and species conditions. The cell voltage is expressed as

$$V_{cell} = E_{rev} + \eta_{act} + \eta_{ohm} + \eta_{conc} \quad (16)$$

where E_{rev} is the reversible voltage and η_{act}, η_{ohm}, and η_{conc} represent the activation, ohmic, and concentration overvoltages, respectively. The resulting local current density links the electrochemical response to the species balances at each node. Gas species are transferred sequentially between adjacent nodes, and the local electrochemical source terms are determined from Faraday's law. The hydrogen production rate is given by

$$\dot{n}_{H_2} = \frac{I}{2F} \quad (17)$$

where I is the current and F is Faraday's constant. In this study, the SOEC model is used to evaluate the steady-state hydrogen-production response of the integrated system, while detailed transient electrochemical behavior is outside the present scope.

3. Simulation results

3.1. Component results

Before constructing the integrated system, the component models were assessed through conservation checks and their steady-state or dynamic responses. The HTGR model, configured using the nominal GT-MHR conditions [19], reached a stable steady state. The SOEC model was previously validated against experimental data from KAERI [18].

The IHX and MHX models were assessed against reference data. Table 2 compares the predicted hot- and cold-side outlet temperatures of the IHX with the

GAMMA results reported in Ref. [6], with the corresponding experimental values included for reference. Across the two operating cases, the present predictions differed from the GAMMA results by 1.9–5.9°C and remained similarly close to the experimental data. The model also reproduced the expected cooling and heating trends on the hot and cold sides, respectively.

Table 2. Comparison of IHX outlet temperatures.

Case / outlet	Experiment [°C]	GAMMA [°C]	Present model [°C]
1 / Hot	72.43	74.69	71.76
1 / Cold	290.32	290.50	292.44
2 / Hot	102.19	103.61	98.32
2 / Cold	510.89	508.89	514.76

For the MHX, predicted outlet temperatures and heat-transfer rates of the helium, steam, and air streams were compared with the reference values of Kim et al. [7] (Table 3). The outlet-temperature differences were 2.7, 7.9, and 3.5°C, respectively, and the corresponding heat-transfer rates differed by 1.2%, 0.2%, and 3.9%. Helium-side heat removal agreed with the combined steam- and air-side gains within 0.01 kW while preserving the expected heat-flow direction. The model therefore reproduced the intended three-stream heat distribution under the reference conditions.

Table 3. Comparison of MHX thermal performance.

Stream	Outlet (T) [°C]		Heat transfer [kW]	
	Reference	Model	Reference	Model
He	564.5	561.8	−10.36	−10.48
Steam	820.0	827.9	+8.05	+8.07
Air	820.0	823.5	+2.31	+2.40

The OTSG and water pump were tested separately under component-level conditions to isolate their transient responses; integrated-system conditions are reported separately. The OTSG used the present 8,572-tube geometry, with helium at 72.2 bar and 270 kg/s and the secondary side at approximately 5 bar. At 100 s, the helium inlet temperature was increased by 2% on an absolute-temperature basis, from 710 to 729.7°C. The superheating region increased from 0.406 to 0.471 m, whereas the boiling region decreased from 1.773 to 1.722 m. The steam outlet temperature rose from 157.6 to 180.6°C without appreciable overshoot, and all three responses settled within approximately 110 s. The gradual response reflects the OTSG thermal phenomena and phase-change energy storage.

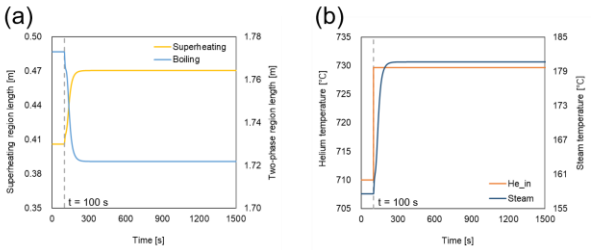


Fig. 4. OTSG response to a helium-temperature step: (a) region lengths and (b) temperature response.

In Fig. 5, the water pump was evaluated between a 1.1-bar source and the 5-bar OTSG inlet. At 50 s, the required flowrate increased by 5%, from 98.98 to 103.93 kg/s. The actual flowrate peaked at 105.66 kg/s at 51.37 s, giving 1.67% overshoot, while motor speed reached 1827.5 rpm at 51.12 s, 0.42% above its final value of 1819.9 rpm. Both responses settled within approximately 4.5 s, with outlet flow converging to the imposed demand. The brief overshoots arise from coupled fluid and shaft inertia before pump head, hydraulic resistance, and rotational torque re-establish equilibrium.

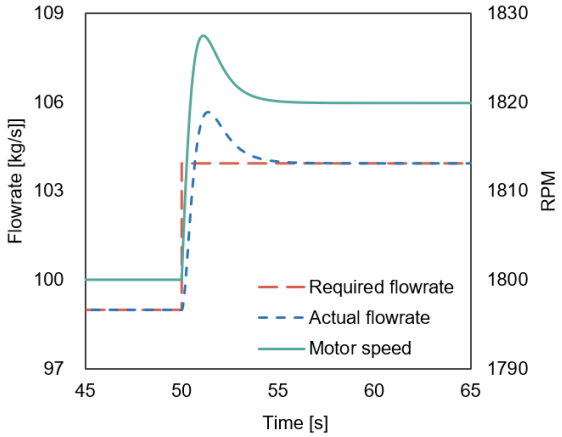


Fig. 5. Water pump response to a 5% step increase.

Transient analysis therefore focuses on the OTSG and water pump, which govern the principal phase-change thermal and feedwater hydraulic–mechanical responses, respectively. The remaining balance-of-plant components are evaluated at the integrated steady state through their stream conditions and associated thermal, separation, and electrochemical functions.

3.2. System results

Table 4 summarizes the steady-state stream conditions of the integrated system, where the helium loops established the intended heat-transfer path and the required SOEC inlet conditions. Under these conditions, the SOEC produced net hydrogen at 8.96 kg/s (358,674 Nm^3/h), with an electrical consumption of 1,200 MW and approximately 96 MW of net electrochemical heat generation associated with operation above the thermoneutral voltage. The resulting specific electricity consumption was 37.23 kWh/kg-H_2, consistent with the

approximately 37 kWh/kg-H_2 reported in large-scale SOEC tests [20].

Table 4. Steady-state stream conditions of the system.

Stream	Fluid	T [°C]	P [bar]	$\dot{m}$ [kg/s]
1	He	872.9	70.2	320
2	He	584.5	70.2	320
3	He	870.7	74.8	270.3
4	He	738.4	74.8	270.3
5	He	529.2	74.8	270.3
6	Air	25	1	94.4
7	Air	33.9	1.1	94.4
8	Air	155	1.1	94.4
9	Air	870.7	1.1	94.4
10	Air/O_2	871.7	1.1	94.4/71.1
11	Air/O_2	805.8	1.1	94.4/71.1
12	Air/O_2	553.6	1.1	94.4/71.1
13	Water	20	1.1	102.4
14	Water	31.1	6.5	138.5
15	Water	63	6.5	138.5
16	Water	142.2	6.5	138.5
17	Steam	156.8	5.4	138.5
18	Steam	520	5.4	138.5
19	Steam	868.6	5.4	138.5
20	Steam	867.9	1.1	138.5
21	H_2/H_2O	62.3	1.1	3.8/9.4
22	H_2/H_2O	885.9	1.1	12.7/67.8
23	H_2/H_2O	561.6	1.1	12.7/67.8
24	H_2/H_2O	61.3	1.1	12.7/67.8
25	H_2/H_2O	62.3	1.1	9/22.3
26	Water	62.3	1.1	36.1

Using the steady-state results, the overall LHV-based energy efficiency was 63.77%. For the exergy analysis, the reactor thermal output was treated as a proxy for the nuclear exergy input under the adopted black-box convention, in which fission exergy is approximated by fission thermal power [21,22]. The resulting H_2-product exergy efficiency was approximately 62.1%. Because the OTSG and fixed nozzle had relatively large exergy destructions, due to finite-temperature-difference heat transfer and throttling, respectively.

4. Conclusion

This study developed a MATLAB/Simulink-based system model of an integrated HTGR–SOEC hydrogen production system, including heat-recovery, water-recycle, and partial hydrogen-recirculation paths. The IHX and MHX showed reasonable agreement with reference thermal data, while the OTSG and water pump exhibited stable transient responses representative of the steam-supply dynamics. System-level energy and exergy analyses were also performed using the steady-state stream results. The developed model provides a basis for further analysis of HTGR–SOEC operation, including system sizing, heat recuperation and efficiency, and load-following operation with external energy sources and coordinated steam-supply and electrolysis control.

REFERENCES

[1] Y. Shin, W. Park, J. Chang, and J. Park, Evaluation of the High Temperature Electrolysis of Steam to Produce Hydrogen, International Journal of Hydrogen Energy, Vol. 32, No. 10-11, pp. 1486-1491, 2007.

[2] J. Kupecki, J. Hercog, K. Motyliński, J. Malesa, D. Muszyński, E. Skrzypek, M. Skrzypek, A. Boettcher, and G. Tchorek, Advancing Production of Hydrogen Using Nuclear Cycles – Integration of High Temperature Gas-Cooled Reactors (HTGR) with Solid Oxide Electrolyzers (SOE), International Journal of Hydrogen Energy, Vol. 53, pp. 40-48, 2024.

[3] Liu, M.; Yu, B.; Xu, J.; Chen, J. Thermodynamic Analysis of the Efficiency of High-Temperature Steam Electrolysis System for Hydrogen Production. J. Power Sources 2008, 177 (2), 493–499.

[4] Z. Dong, Dynamical Modeling and Coordinated Control Design of a Multimodular Nuclear Power-Hydrogen Cogeneration Plant, Energy Conversion and Management, Vol. 272, 116369, 2022.

[5] L. C. Juárez-Martínez and G. Espinosa-Paredes, Development of a Zero-Dimensional Dynamic Simulator of a Power Conversion System with a High-Temperature Gas Reactor, International Journal of Energy Research, Vol. 45, No. 11, pp. 16984-16994, 2021.

[6] I. H. Kim, H. C. No, J. I. Lee, and B. G. Jeon, Thermal Hydraulic Performance Analysis of the Printed Circuit Heat Exchanger Using a Helium Test Facility and CFD Simulations, Nuclear Engineering and Design, Vol. 239, No. 11, pp. 2399-2408, 2009.

[7] S.-Y. Kim, B. H. Park, S.-D. Hong, and C. S. Kim, Experimental Performance Evaluation of a Multi-Stream Heat Exchanger for Integration of High-Temperature Steam Electrolysis with Nuclear Reactor Systems, Korean Journal of Chemical Engineering, Vol. 41, No. 10, pp. 2901-2912, 2024.

[8] H. Li, X. Huang, and L. Zhang, A Lumped Parameter Dynamic Model of the Helical Coiled Once-Through Steam Generator with Movable Boundaries, Nuclear Engineering and Design, Vol. 238, No. 7, pp. 1657-1663, 2008.

[9] S. Wu, Z. Li, P. Wang, G. H. Su, and J. Wan, A Three-Region Movable-Boundary Helical Coil Once-Through Steam Generator Model for Dynamic Simulation and Controller

Design, Nuclear Engineering and Technology, Vol. 55, No. 2, pp. 460-474, 2023.
[10] Y. Mori and W. Nakayama, Study on Forced Convective Heat Transfer in Curved Pipes, International Journal of Heat and Mass Transfer, Vol. 10, No. 5, pp. 681-695, 1967.
[11] W. M. Rohsenow, A Method of Correlating Heat-Transfer Data for Surface Boiling of Liquids, Transactions of the ASME, Vol. 74, No. 6, pp. 969-975, 1952.
[12] N. Zuber, On the Stability of Boiling Heat Transfer, Transactions of the ASME, Vol. 80, pp. 711-720, 1958.
[13] P. J. Berenson, Film-Boiling Heat Transfer from a Horizontal Surface, Journal of Heat Transfer, Vol. 83, No. 3, pp. 351-358, 1961.
[14] L. A. Bromley, Heat Transfer in Stable Film Boiling, Chemical Engineering Progress, Vol. 46, No. 5, pp. 221-227, 1950.
[15] Gnielinski, V. New Equations for Heat and Mass Transfer in Turbulent Pipe and Channel Flow. Int. Chem. Eng. 1976, 16 (2), 359–368.
[16] Chilton, T. H.; Colburn, A. P. Mass Transfer (Absorption) Coefficients Prediction from Data on Heat Transfer and Fluid Friction. Ind. Eng. Chem. 1934, 26 (11), 1183–1187.
[17] Schiller, L.; Naumann, A. Über die grundlegenden Berechnungen bei der Schwerkraftaufbereitung. Z. Ver. Dtsch. Ing. 1933, 77, 318–320.
[18] J. Ahn, B. H. Park, and H. K. Cho, Efficient Numerical Modeling and Parametric Analysis of Solid Oxide Electrolysis Cells and Stacks for Nuclear Hydrogen Production, International Journal of Energy Research, Vol. 2025, Article ID 4254549, 18 pages, 2025.
[19] Baxi, C. B.; Shenoy, A.; Kostin, V. I.; Kodochigov, N. G.; Vasyaev, A. V.; Belov, S. E.; Golovko, V. F. Evaluation of Alternate Power Conversion Unit Designs for the GT-MHR. Nucl. Eng. Des. 2008, 238 (11), 2995–3001. DOI: 10.1016/j.nucengdes.2007.12.021.
[20] Casteel, M. J.; Westover, T. L.; Shigrekar, A.; Olowu, T.; Ta, A.; Lavernia, A.; Zargari, A.; Cheldelin, B. Ultra-High Efficiency Hydrogen Production Using a Large-Scale Solid Oxide Electrolysis Cell System. Int. J. Hydrogen Energy 2025, 157, 150283.
[21] L. Ferroni and A. Natale, “Exergy Analysis of a PWR Nuclear Steam Supply System – Part I, General Theoretical Model,” Energy Procedia, Vol. 148, pp. 1230–1237, 2018.
[22] M. A. Rosen, “Energy- and Exergy-Based Comparison of Coal-Fired and Nuclear Steam Power Plants,” Exergy, An International Journal, Vol. 1, No. 3, pp. 180–192, 2001.